

Article

Porous Cu(Mn)-Doped ZnO-MgO Nanocomposites for Photocatalytic and Antibacterial Applications

Andrey Shelemanov ¹, Marianna Gavrilova ², Sergey Evstropiev ^{1,2,*}, Anna Karavaeva ³ and Vyacheslav Samonin ⁴

¹ Scientific and Educational Center of Photonics and Optoinformatics, ITMO University, Kronverskii pr., 49, Saint Petersburg 197101, Russia; shelemanov@mail.ru (A.S.)

² Department of Chemical Technology of Refractory Non-Metallic and Silicate Materials, Saint-Petersburg State Institute of Technology (Technical University), Moscovskii pr., 13, Saint Petersburg 190013, Russia; amonrud@yandex.ru (M.G.)

³ Department of Microbiology, Saint-Petersburg State Chemical-Pharmaceutical University, Prof. Popov Str., 14, Saint Petersburg 197376, Russia; ann-karavaeva@yandex.ru (A.K.)

⁴ Department of Chemistry and Technology of Materials of Sorption Engineering, Saint-Petersburg State Institute of Technology (Technical University), Moscovskii pr., 13, Saint Petersburg 190013, Russia; samonin@spbti.ru (V.S.)

* Corresponding author. E-mail: evstropiev@bk.ru (S.E.)

Received: 13 November 2024; Accepted: 17 February 2025; Available online: 21 February 2025

ABSTRACT: Porous Cu(Mn):ZnO-MgO composites synthesized by polymeric sol-gel method were characterized. The crystal structure, morphology, spectral properties, the ability of the photogeneration of chemically active singlet oxygen under external visible irradiation, photocatalytic and antibacterial properties of porous composites were studied. Obtained composites consist of small ZnO and MgO crystals having size less than 20 nm. It was found that Cu²⁺ and Mn²⁺ ions are embedded into the lattices of ZnO and MgO crystals, altering their crystal cell parameters. The band gap values of obtained composites are 3.41 ÷ 3.42 eV which are slightly higher than the band gap of pure ZnO. Prepared materials demonstrate a high ability of photogeneration of chemically active singlet oxygen under blue light ($\lambda = 405$ nm) irradiation. It was found that dependencies of the intensity of singlet oxygen photogeneration from the power density of visible irradiation are linear. Photocatalytic decomposition of the diazo dye Chicago Sky Blue in solutions under UV and blue light irradiation proceeds rapidly in the presence of the prepared composites (constants rate of photocatalytic dye decomposition under UV irradiation are 0.024 min⁻¹ and 0.025 min⁻¹ for ZnO-MgO composites doped with Cu and Mn, correspondingly). Porous composites demonstrate superior antibacterial activity against gram-positive bacteria. These materials are promising for practical application in medicine and photocatalytic technologies of air and water cleaning.

Keywords: Photocatalysis; Singlet oxygen; Composite; Sol-gel



© 2025 The authors. This is an open access article under the Creative Commons Attribution 4.0 International License (<https://creativecommons.org/licenses/by/4.0/>).

1. Introduction

Environmental problems worldwide stimulate the study and development of new photocatalytic and bactericidal materials. Many semiconductor oxide materials (such as TiO₂, ZnO and SnO₂) demonstrate high photocatalytic properties and antibacterial activity [1–4]. These materials are characterized by thermal stability and chemical durability and can be synthesized using different facile methods.

The main mechanism of photocatalytic effect and antibacterial activity of metal oxide is the generation of reactive oxygen species (ROS) under external irradiation and the following oxidation by organic compounds [5,6]. The photogeneration of ROS is determined by the photocatalyst properties (chemical composition; morphology; presence of structural defects) and the characteristics of external irradiation (wavelength; power density of excited light) [1,2]. The ROS generation occurs on the surface of semiconductors and the materials with high specific surface areas (different nanostructures; porous matrixes) demonstrate enhanced photocatalytic and bactericidal properties [7–10]. The increase of the intensity of the exciting light enhances the ROS generation and accelerates photocatalytic processes [2,11,12].

The adsorption of organic compounds from the gas or liquid phases on the surface of the photocatalyst is considered the preliminary stage of their photocatalytic decomposition. The adsorption processes of the organic compounds on the

surface of different photocatalysts were studied in many works [8,9,13–16]. It was found that the adsorption proceeds especially effectively on the materials with high specific surface area that enhanced additionally their photocatalytic characteristics. The adsorption and photocatalytic phenomena using different porous materials were described in [13–18].

The materials based on ZnO are highly effective photocatalysts and demonstrate antibacterial activity [3,4,7,8]. Pure ZnO nanoparticles have relatively high band gap values of $3.1 \div 3.37$ eV [4,8] and show high photocatalytic properties under UV irradiation.

Different additives to ZnO are used to enhance photocatalytic activity under visible light irradiation, improve antibacterial properties, and reduce the recombination of photogenerated electron-hole pairs [8,19–23]. The mechanism of the significant improvement of photocatalytic and antibacterial activity of ZnO by these additions includes as the optimization of material electronic structure and the formation of semiconductor heterostructures so as the decrease of crystal sizes in the obtained nanocomposites [24,25]. The last phenomenon was observed in the ZnO-based composites and related to the mutual inhibition of the simultaneous growth of different crystals during composites fabrication [24].

ZnO-MgO composites exhibit high adsorptive properties and photocatalytic activity under UV irradiation. The spectral and luminescent properties of these composites, their morphology, crystal parameters, and electronic structure were studied previously in many works [13,24–35]. According to [33], ZnO-MgO composites demonstrate higher photocatalytic and bactericidal properties than pure ZnO and MgO oxides. The literature data show that the morphology, electronic structure, and properties of ZnO-MgO composite depend on the method of their synthesis [24,26].

Different methods (hydrothermal [33], sol-gel [8,18,30,34–38], metal-organic decomposition [28]) have been used for the synthesis of ZnO-MgO nanocomposites. The polymeric sol-gel method is simple, cheap, and provides the fabrication of photocatalytic composites [8,10,18,37].

ZnO-MgO nanocomposites have high band gap values ($3.20 \div 3.28$ eV [32]) and demonstrate high photocatalytic properties under UV irradiation [34,39]. The modification of ZnO-MgO composites by Ag was used to enhance their photocatalytic and bactericidal properties [22]. The oxides of transition metals (Cu, Fe, Mn) are often added to ZnO-based materials to improve photocatalytic properties and antibacterial activity [39–42]. These additions can change the electronic structure of ZnO-based materials and enhance their photocatalytic activities under visible irradiation.

Highly effective porous ZnO-based photocatalysts have been synthesized and studied in [8,10,18]. A facile polymeric sol-gel method was applied in [8,10,15] to fabricate porous ZnO-based photocatalysts. It was found [8,18] that the rate of organic contamination decomposition is significantly (about 2 times) faster in the presence of porous photocatalysts compared with grainy non-porous counterparts. These results determine the prospects of the application of the polymer-salt method for the synthesis of highly effective porous photocatalysts.

It is known [43,44] that diazo dyes are widely used in the textile, paints and plastics industries and are the hazard contamination of its wastewater. Therefore, the study of their photocatalytic decomposition in the presence of developing composites is an actual problem.

The aim of this work is to synthesize porous photoactive Mn- and Cu-doped ZnO-MgO composites using the polymeric sol-gel method and to characterize their crystal structure, morphology, band gap values, photogeneration ability of chemically active singlet oxygen, as well as their photocatalytic and bactericidal activities.

2. Materials and Methods

In this work, the sol-gel method was used to synthesize ZnO-based composites. Aqueous solutions of metal nitrates were mixed with a solution of polyvinylpyrrolidone (PVP, $M_w = 25,000 \div 35,000$) and stirred at room temperature using a magnetic stirrer until the nitrates were completely dissolved and a heterogeneous solution was formed. All metal nitrates used were of analytical grade (Neva-Reaktiv (Saint Petersburg; Russia)). Then the solutions were dried in an incubation cabinet in an air atmosphere at 70 °C for 5 days until the gel was completely solidified. The resulting gel was calcined at 550 °C for 2 h in a muffle furnace under an air atmosphere. The resulting materials were light white powders.

The morphology of the obtained composites was studied by SEM analysis using the instrument TESCAN MIRA3 (TESCAN, Brno, Czech Republic) equipped with the setup EssenceTM for energy-dispersive X-ray analysis (EDXA). Analytical chemical compositions of prepared composites and their elemental compositions are given in Tables 1 and 2. Further, the ZnO-MgO nanocomposite doped with Cu and Mn will be designated as ZnMgCu and ZnMgMn correspondingly.

Table 1. Analytical chemical composition of obtained composites.

| Components | Components, wt.% | | | |
|------------|------------------|------|-----|------------------|
| | ZnO | MgO | CuO | MnO ₂ |
| ZnMgCu | 65.6 | 33.3 | 1.1 | - |
| ZnMgMn | 64.3 | 34.8 | - | 0.9 |

Table 2. Elemental chemical compositions of composites.

| Composite | ZnMgCu | | | ZnMgMn | | |
|--------------------|--------|------|-------|--------|------|-------|
| | Mg | Cu | Zn | Mg | Mn | Zn |
| Element | | | | | | |
| Max, at. % | 51.50 | 0.88 | 50.07 | 52.17 | 0.59 | 47.50 |
| Min, at. % | 49.05 | 0.81 | 47.69 | 52.07 | 0.43 | 47.24 |
| Mean, at. % | 50.22 | 0.84 | 48.93 | 52.14 | 0.51 | 47.36 |
| Standard deviation | 1.23 | 0.04 | 1.19 | 0.06 | 0.08 | 0.13 |

The crystal structure of prepared powders was studied by XRD method using device Rigaku Ultima IV (Rigaku Corporation, Akishima, Japan). The used scanning parameters were: CuK_α radiation ($\lambda = 1.54056 \text{ \AA}$), 40 kV, 30 mA, a scan speed of $2^\circ/\text{min}$, and the step width was 0.01° . The diffraction patterns were scanned from 30° to 100° (2θ). Based on the obtained XRD data, we estimated the crystal sizes by the application of Scherrer's formula:

$$d = \frac{K \times \lambda}{\beta \times \cos\theta'} \quad (1)$$

where d is the average crystal size; K is the dimensionless particle shape factor (for spherical particles $K = 0.9$); λ is the X-ray wavelength (λ (CuK_α = 1.5418 \AA); β —is the width of the reflection at half height (in radians, and in units of 2θ); θ is the diffraction angle. The unit cell parameters were calculated using the Rietveld method.

Diffusion reflectance spectra were measured using spectrophotometer Perkin Elmer Lambda 900 (PerkinElmer Inc., Waltham, MA, USA). Function Kubelka-Munk (F_{KM}) was used to analyze diffuse reflection spectra. F_{KM} is proportional to the optical absorption coefficient of the material and can be obtained using the expression:

$$F_{KM} = \frac{(1 - R^2)}{2R}, \quad (2)$$

where R is the diffuse reflectance of the material, measured relative to completely white body.

The Tauc equation was used to evaluate the band gap values of obtained composites. This equation can be written as [9]:

$$(F_{KM} \cdot hv)^2 = A(hv - E_g), \quad (3)$$

where hv —photon energy, E_g —band gap value, A —constant, F_{KM} —Kubelka-Munk function. The graphs $(F_{KM} \times hv)^2$ vs. hv were plotted to determine E_g values. The possibility of the application of Equation (3) for the determination of band gap values of doped ZnO composites was discussed in detail in [45]. In this study Equation (3) was used only for the estimation of E_g values to determine the possible spectral range of high photocatalytic activity of composites.

Chemically active singlet oxygen demonstrates the characteristic photoluminescence in NIR spectral range ($\lambda_{\text{max}} = 1270 \text{ nm}$) under external irradiation [3]. In this work we used this luminescent method described in [3] to study the photogeneration of singlet oxygen by prepared composites under visible irradiation using LED (HPR40E set) ($\lambda_{\text{max}} = 405 \text{ nm}$).

Aqueous solutions of diazo dye Chicago Sky Blue (CSB) (Sigma Aldrich, St. Louis, MO, USA) were applied as a model of organic contamination in our photocatalytic experiments. CSB was used previously for the estimation of the photocatalytic properties of different oxide materials [8,18]. The photocatalytic properties of powders were studied in their suspensions which were prepared by the addition of 0.01 g of the composite to 3 mL of the aqueous solution of Chicago Sky Blue (CSB) dye (0.01 g/L). The dye content in the initial solutions was 41 mg/L.

The mercury lamp (DR-240, Saransk, Russia) and LED Tresbro UV Resin Curing Light-01 ($\lambda_{\text{max}} = 405 \text{ nm}$) were used for light irradiation of the cuvette with dye solution. The maximal wavelength of the radiation of this mercury lamp is 254 nm. The full emission spectrum of this lamp was given in [46]. The cuvette was disposed of at the distance 7 cm from the light source. The power density of the LED radiation during photocatalytic experiments was 0.6 W/cm^2 . The radiation energy densities were 0.2 W/cm^2 (mercury lamp) and 0.7 W/cm^2 (LED) during the photocatalytic test for CSB photodecomposition in the solutions. During photocatalytic experiments CSB contents in solutions were

determined by periodical measurements of their absorption spectra using the spectrophotometer Perkin Elmer Lambda 650 UV/VIS.

Antibacterial activity of composites was studied under ambient lighting in this work. The method described in [19] was used to estimate the antibacterial activities of synthesized oxide materials. The gram-positive bacteria *Staphylococcus aureus* ATCC 209P and gram-negative bacteria *Escherichia coli* ATCC 25922 were used as test bacteria. Antibacterial tests were performed in natural lighting conditions (illuminance about 1500 lux). In antibacterial tests equal amounts of each powder composite (0.5 g) were divided into three parts and put into Petri dish. So, six pills (three of each composite) were used simultaneously in antibacterial tests. The antibacterial effect was studied by measuring the size of an inhibited area, which is formed on a surface containing bacteria. The size of an inhibited area was determined as the average thickness of the zone around the powder sample that is free from bacteria.

The bactericidal tests included a few following stages:

1. Agar was prepared from the dry powder as a nutrient material and tested for sterility and growth ability. The prepared agar was melted in a water bath, poured 20 mL into sterile Petri dishes with a diameter of 90 mm and left to harden at a temperature of 20 °C.
2. A pure daily culture of microorganisms was used to prepare the inoculum. The material was transferred with a loop into a bottle with a sterile saline solution, bringing the inoculum density to 1×10^9 CFU/mL according to the bacterial turbidity standard.
3. The inoculum was spread with a spatula over the entire surface of the agar in Petri dish.
4. Powdered samples were applied to the surface of the medium using sterile tweezers and measuring spoons no later than 15 min after inoculation. Next, Petri dishes with the inoculant, agar, and a powder sample of the nanocomposite were incubated at room temperature for 24 h. After incubation, the dishes were placed upside down on a dark matte surface. The angle of incidence of light was 45°. Then the sizes of the inhibitory zone (zone without bacteria) were measured.

3. Results and Discussions

3.1. XRD Analysis

Figure 1 shows XRD patterns of obtained composites. Intensive peaks of wurtzite hexagonal ZnO crystals are observed in both diffractograms. The calculations carried out by using Scherrer's formula showed that the average size of ZnO crystals was less than 20 nm in both ZnMgCu and ZnMgMn composites.

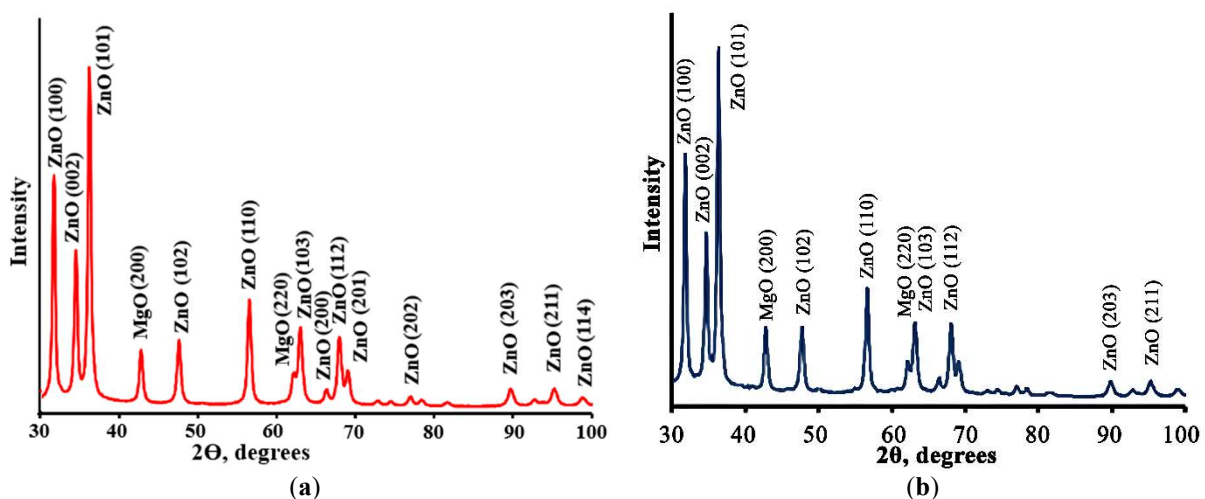


Figure 1. XRD pattern of powders ZnMgMn (a) and ZnMgCu (b).

Small peaks of cubic MgO crystals (periclase) (ICSD 166273) are also observed in these patterns. XRD patterns showed the absence of any peaks of Mn or Cu compounds that can be related to the small content of these components to the embedding of Mn and Cu ions into the structure of ZnO crystals.

The experimental data showed that the peak positions in XRD patterns of obtained composites are slightly different (Table 3). The peaks in the XRD pattern of ZnMgMn powder are located at smaller 2θ values than in the diffractogram of ZnMgCu sample. The variation of the peaks position indicates the difference of the parameters of ZnO crystal cells in obtained composites.

Table 3. The positions of the most intensive peaks of ZnO crystals in XRD patterns of obtained composites.

| (hkl) | ZnMgCu | ZnMgMn |
|-------|-------------|--------|
| | 2θ, Degrees | |
| (100) | 31.77 | 31.73 |
| (002) | 34.60 | 34.45 |
| (101) | 36.30 | 36.29 |
| (102) | 47.68 | 47.58 |
| (110) | 56.60 | 56.66 |

Zn²⁺ ions in wurtzite hexagonal ZnO crystals are in tetrahedral coordination and the ionic radius of Zn²⁺(IV) is 0.6 Å. Mg²⁺(IV), Mn²⁺(IV) and Cu²⁺(IV) ions have ionic radii 0.57; 0.66 and 0.57 Å, correspondingly [47] and can substitute zinc ions in the lattice of ZnO crystals [31,35,42,48]. The replacement of Zn²⁺ ions by bigger ones can be accompanied by some deformation of ZnO crystal lattice. So, some expansion of ZnO crystal cells at the embedding of Ag⁺ ions having ionic radii bigger than that Zn²⁺ ions were observed earlier in [10,49]. The embedding of Cu ions into ZnO crystal lattices also leads to some of their distortion [50].

Table 4 shows the calculated ZnO crystal cell parameters in the composites and different literature data on these values in pure ZnO. The volumes of crystal cells of ZnO crystals in Mn-doped composites are bigger than in pure ZnO. This fact suggests embedding Mn²⁺ ions into the structure of ZnO crystals in ZnMgMn composite. This assumption agrees with the results reported previously in [51]. The scheme illustrating the embedding of Mn²⁺ ions into the ZnO crystals is shown in Figure 2a. Also, it is worth noting that the comparison of ZnO crystal cell parameters in composites obtained in this study with the data given in [51] for composite Zn_{0.91}Mg_{0.09}Ag_{0.01}O shows that their values are similar.

Table 4. Parameters of ZnO crystal cells in different materials.

| Sample | a, Å | c, Å | V, Å ³ | c/a | Reference |
|--|--------|--------|-------------------|--------|------------------|
| ZnMgMn | 3.2563 | 5.2000 | 47.7483 | 1.5969 | Present study |
| ZnMgCu | 3.2447 | 5.1800 | 47.2277 | 1.5964 | Present study |
| Zn _{0.91} Mg _{0.09} Ag _{0.01} O | 3.2465 | 5.1879 | 47.355 | 1.5980 | [50] |
| ZnO | 3.25 | 5.21 | 47.85 | 1.603 | [47] |
| ZnOAg | 3.25 | 5.21 | 48.01 | 1.603 | [47] |
| ZnO | 3.2535 | 5.2151 | 47.81 | - | ICSD code 067848 |
| ZnO | 3.2496 | 5.2042 | - | 1.6018 | [48] |
| ZnO | 3.2501 | 5.2071 | 47.63 | 1.6021 | [49] |
| ZnO | 3.249 | 5.205 | 54.9 | 1.6020 | [36] |
| Zn _{0.99} Mn _{0.01} O | 3.2500 | 5.2030 | 47.59 | 1.6009 | [51] |
| Zn _{0.95} Mn _{0.05} O | 3.2493 | 5.2023 | 47.57 | 1.6010 | [51] |
| Cu _{0.0417} Zn _{0.9583} O | 3.272 | 5.284 | 61.2 | 1.5967 | [36] |
| Cu _{0.0278} Zn _{0.9722} O | 3.249 | 5.205 | 54.9 | 1.6020 | [36] |

The volume of ZnO crystal cells in the composite ZnMgCu is less than in pure ZnO, that can be explained by the replacement of Zn²⁺ by the smaller ions Cu²⁺. This phenomenon was observed earlier in [39].

Mg²⁺ ions in cubic MgO crystals are in octahedral coordination and ionic radius Mg²⁺(VI) is 0.72 Å [47]. Zn²⁺(VI), Mn²⁺(VI) and Cu²⁺(VI) ions have ionic radii 0.74; 0.83 and 0.73 Å, correspondingly [47] and can substitute Mg²⁺ ions in the structure of cubic MgO crystals. Table 5 shows the positions of peaks of MgO crystals in XRD patterns of obtained composites and calculated crystal cell parameters. MgO peaks are shifted into the smaller 2θ values in XRD patterns of composites compared with standard values (ICSD code 166273). This fact suggests that Mg²⁺ ions could be substituted by the bigger ions (Zn²⁺, Mn²⁺ or Cu²⁺) and MgO crystal cell was expanded. The scheme illustrating the embedding of Mn²⁺ ions into the MgO crystals is shown in Figure 2b.

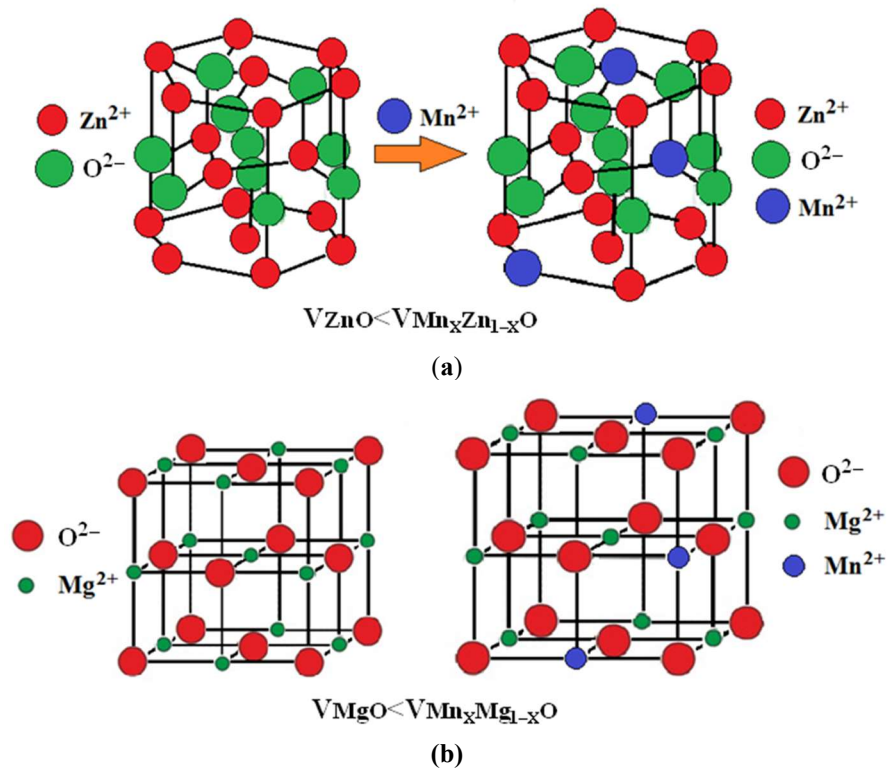


Figure 2. (a) Scheme illustrating the embedding of Mn^{2+} ions into the ZnO crystals. (b) Scheme illustrating the possible embedding of Mn^{2+} ions into the MgO crystals.

Table 5. The positions of the most intensive peaks of MgO crystals in XRD patterns of obtained composites.

| Crystal Cell Parameters | (hkl) | ICSD 166273 | ZnMgCu | ZnMgMn |
|-------------------------|-------|----------------------|--------|--------|
| | | 2 θ , Degrees | | |
| | (111) | 37.04 | 36.82 | 36.82 |
| | (200) | 43.04 | 42.78 | 42.77 |
| | (220) | 62.49 | 62.10 | 62.08 |
| | (311) | 74.93 | 74.42 | 74.41 |
| | (222) | 78.89 | 78.35 | 78.33 |

Clearly, that the absence of peaks of Mn and Cu compounds and observed peaks positions shifts are not the strong evidence of the embedding of doping ions into ZnO and MgO crystal lattices. However, the obtained data from XRD analysis allows the assumption that the doping additions of Cu^{2+} and Mn^{2+} modify and deform the structure of ZnO and MgO crystals.

3.2. Morphology of Composites

Figure 3 demonstrates SEM photos of ZnMgMn (a) and ZnMgCu (b) composites. Both composites have porous structures related to the use of PVP additions, providing gas product generation during the calcination stage during composites synthesis. Composites structures are composed of aggregates having a size < 100 nm.

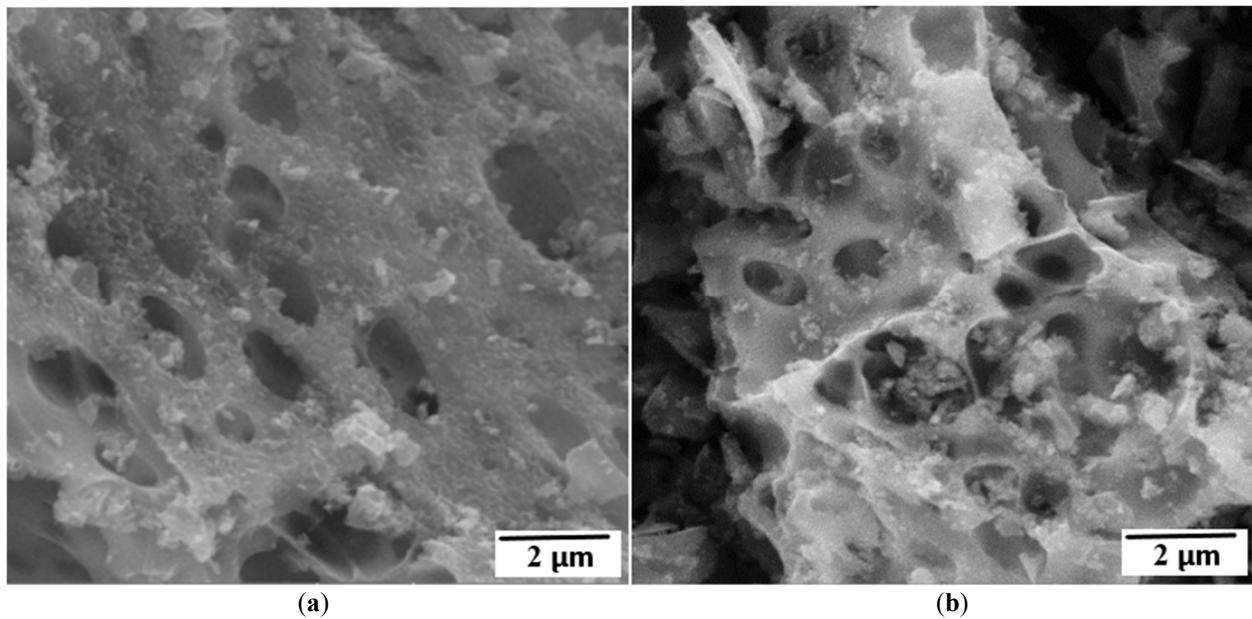


Figure 3. SEM photos of ZnMgMn (a) and ZnMgCu (b) composites.

This porous materials morphology provides them with high specific surface areas and effective contact with the surrounding media. The data of BET method (argon adsorption) show that the values of specific surface areas of powders are $5.6 \text{ m}^2/\text{g}$ and $7.8 \text{ m}^2/\text{g}$ for ZnMgMn and ZnMgCu samples, correspondingly.

3.3. Spectral Properties of Composites

Figure 4 shows diffuse reflection spectra of composites ZnMgMn (curve 1) and ZnMgCu (curve 2). The observed significant decrease of the reflection at $\lambda < 400 \text{ nm}$ is related with the absorption edge of ZnO crystals.

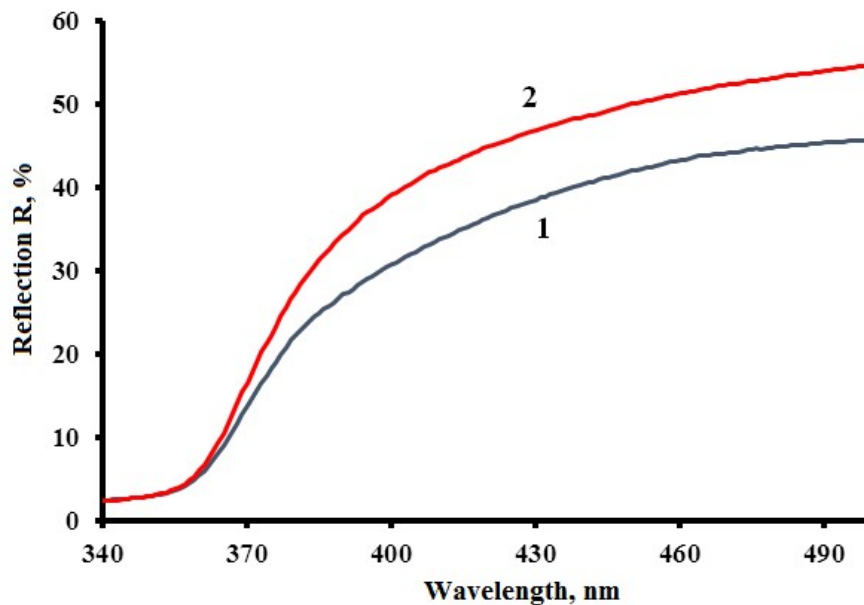


Figure 4. Diffuse reflection spectra of composites ZnMgMn (curve 1) and ZnMgCu (curve 2).

The dependencies $(F_{KM}h\nu)^2 = f(h\nu)$ obtained for composites ZnMgCu (a) and ZnMgMn (b) are shown in Figure 5. Obtained E_g values are 3.42 and 3.41 eV for composites ZnMgCu and ZnMgMn, correspondingly. These values are higher than the band gap values of ZnO nanocrystals ($3.10 \div 3.37 \text{ eV}$ [8,40]) and ZnO-MgO nanocomposites ($3.20 \div 3.28 \text{ eV}$ [33]). In spite of these values being estimated only, obtained results suggest that UV irradiation is preferable for the effective excitation of composites.

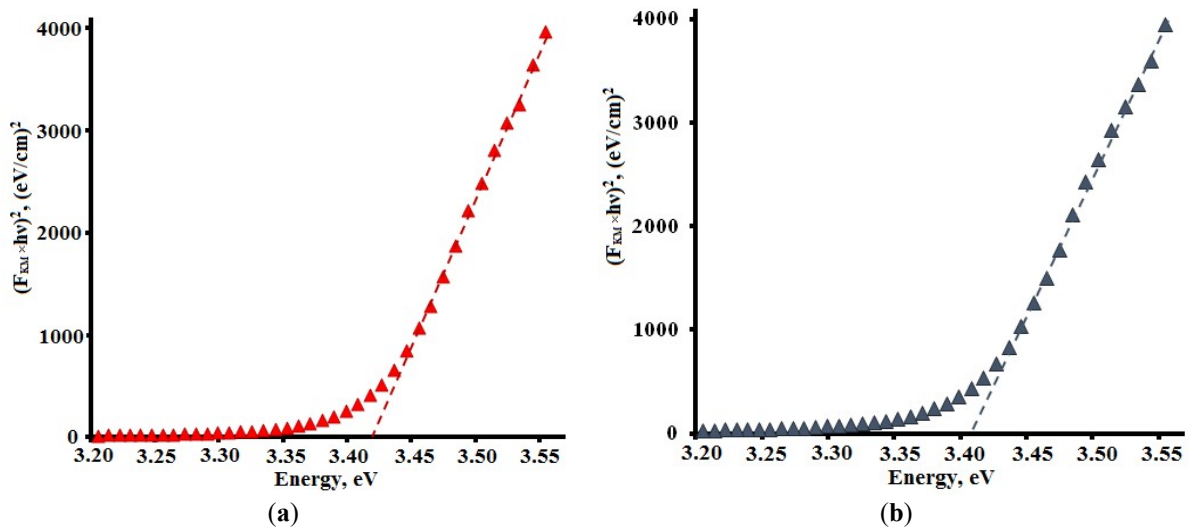


Figure 5. The dependencies $(F_{KM}hv)^2 = f(hv)$ obtained for composites ZnMgCu (a) and ZnMgMn (b).

3.4. Singlet Oxygen Photogeneration

It is known that singlet oxygen is one of the most chemically active oxygen species. It is generated by photocatalytic materials and actively taking part in their antibacterial activity and the photodecomposition of organic contaminations.

Figure 6a shows photoluminescence spectrum of ZnMgMn composite in NIR spectral range. Characteristic luminescence band with $\lambda_{\max} = 1270$ nm attributed to the singlet oxygen is observed in the spectrum. It is worth to notice that this luminescence is observed at the excitation of the composite by the blue light ($\lambda_{\text{ex}} = 405$ nm) with the photon energy 3.06 eV that is less than the band gap value of ZnMgMn composite ($E_g = 3.41$ eV). This phenomenon can be attributed to the effect of structural defects which are often present in highly dispersive materials and play a key role in the generation of ROS and in the photocatalytic processes [4,7,9,52].

The dependencies of the luminescence intensities of singlet oxygen photogenerated by the powders ZnMgCu (curve 1) and ZnMgMn (curve 2) from the excited light ($\lambda = 405$ nm) power density are shown in Figure 6b. The growth of power density of the excited light increases the intensity of the singlet oxygen emission, and the dependencies shown in Figure 6b are almost linear. Similar results were obtained earlier for the singlet oxygen generation by the porous ZnO powder [8]. Also, it is worth noticing that the linear dependencies of the constant rate k of organics photocatalytic degradation from the visible light intensity I_{ex} were observed in [12]. The deviations from the linearity of these dependencies were observed at the high I_{ex} values [1,12].

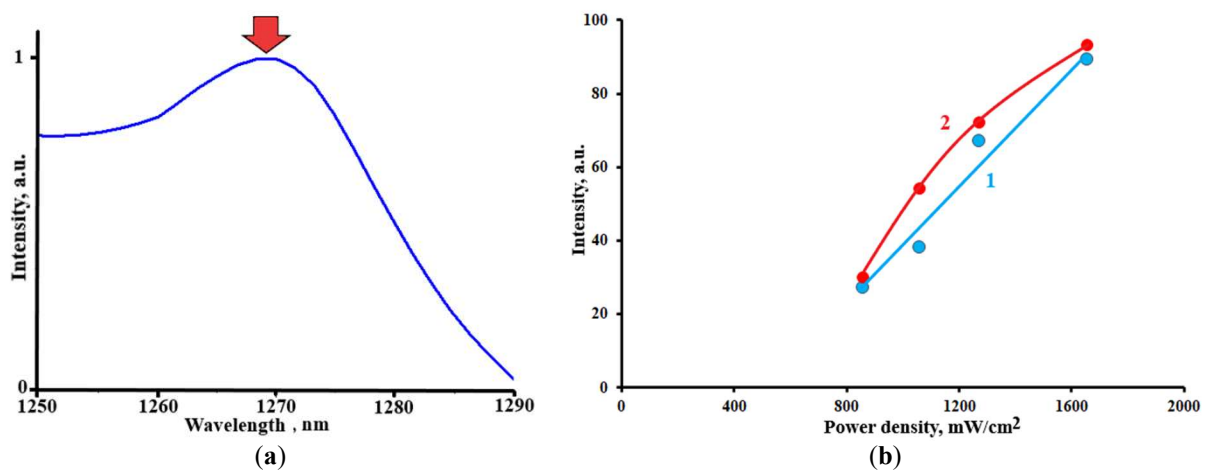


Figure 6. (a) Photoluminescence spectrum of ZnMgMn composite in NIR spectral range. Luminescence excitation wavelength 405 nm. The excited light powder density 1670 W/cm²; (b) The dependencies of the luminescence intensities of singlet oxygen photogenerated by the powders ZnMgCu (curve 1) and ZnMgMn (curve 2) from the excited light ($\lambda = 405$ nm) power density.

3.5. Kinetics of Dye Photocatalytic Decomposition

The experiments showed that obtained composites demonstrate high photocatalytic activity for the CSB decomposition. The kinetics of CSB dye photolysis under UV and blue light irradiation in solution without any additions is shown in Figure 7a,b. The decreases of CSB content in solution by the dye photolysis without photocatalytic additions are negligible at the application of both UV and blue light irradiations.

Figure 7 also demonstrates the kinetics dependencies of photocatalytic decomposition of CSB dye in solutions in the presence of powders of ZnMgCu (curve 2) ZnMgMn (curve 3) and under UV (Figure 7a) and visible (Figure 7b) irradiations. UV irradiation of dye solutions with ZnMgCu and ZnMgMn composites additions for 30 min leads to the decomposition of about 50% of CSB molecules.

Observed rates of photocatalytic dye decomposition are remarkably higher at the application of blue LED as the light source, that is explained by its significantly higher power density of radiation (see Section 2).

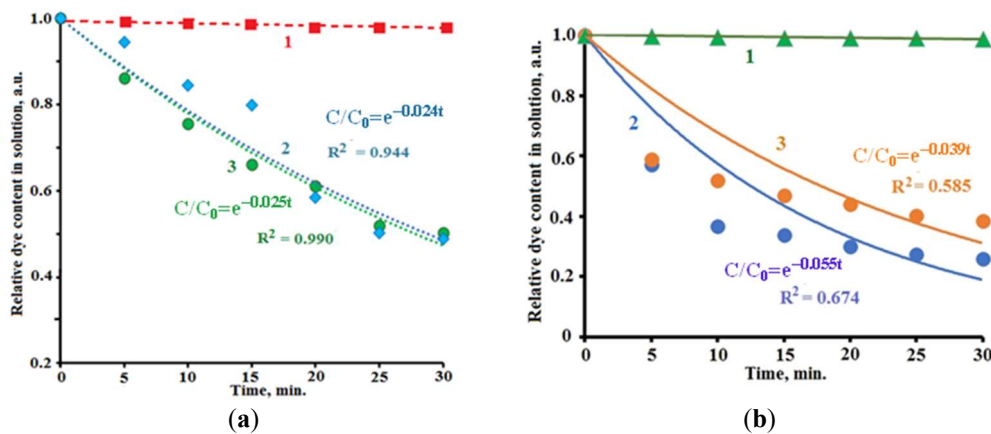


Figure 7. Kinetics dependencies of dye photolysis in the solution without any additions (curves 1; Figure 7a,b) and photocatalytic decomposition of CSB dye in solutions at the presence of powders of ZnMgCu (curves 2; Figure 7a,b), ZnMgMn (curves 3; Figure 7a,b). Excitation of composites by UV (a) or by blue light (b).

The kinetic equation of pseudo-first order, which is often used in photocatalysis in integral form, can be written as [8]:

$$C/C_0 = e^{-kt}, \quad (4)$$

where C_0 and C —initial and current dye concentrations (mM); t —duration of UV irradiation (min); and k —reaction rate constant (min^{-1}). The calculations showed that the Equation (4) successfully describe experimental results ($R^2 > 0.9$).

The comparison of obtained values of constant rates of CSB decomposition k with the literature data related to the photocatalytic decomposition of this dye is given in Table 6. The rates of CSB photocatalytic decomposition observed in the presence of prepared Cu- and Mn-doped ZnO-MgO composites are similar to the values for the grainy ZnO powder and ZnO 80.16 mol.% + ZnAl₂O₄ 19.83 mol.% + CuO 0.04 mol. % composite, given in [8,18]. These k values are significantly higher than the rate constant observed in [18] for composite ZnO 20.81 mol. % + ZnAl₂O₄ 79.18 mol.% + CuO 0.01 mol. %. However, the rate constants of dye decomposition obtained in this study are significantly lower than k values reported for porous ZnO powder ([8]) and ZnO nanoflowers ([48]).

This comparison demonstrates the important roles of high ZnO content and optimized morphology (porous structure; nanoflowers) in the formation of highly effective ZnO-based photocatalysts. It is worth noticing that this conclusion was made for the photocatalytic decomposition of CSB under UV irradiation.

Table 6. Rate constants of CSB photocatalytic decomposition under UV irradiation.

| Material | Photocatalysts Constant Rate, min^{-1} | References |
|--|---|--------------|
| Grainy powder ZnO | 0.025 | [8] |
| Porous powder ZnO | 0.042 | [8] |
| ZnO nanoflowers | 0.032 | [48] |
| Powder ZnO 80.16 mol.% + ZnAl ₂ O ₄ 19.83 mol.% + CuO 0.04 mol.% | 0.021 | [18] |
| Powder ZnO 20.81 mol.% + ZnAl ₂ O ₄ 79.18 mol.% + CuO 0.01 mol.% | 0.005 | [18] |
| ZnMgCu | 0.024 | present work |
| ZnMgMn | 0.025 | present work |

Figure 7b shows the kinetic dependencies of CSB photocatalytic decomposition in the presence of obtained composites under blue light irradiation. The rates of dye photocatalytic decomposition under blue light irradiation are remarkably higher than that observed under UV radiation. This fact is related to the higher power density of the radiation when the LED is applied.

3.6. Antibacterial Activity

Figure 8 demonstrates photos of Petri dishes with agar containing gram-positive bacteria *Staphylococcus aureus* ATCC 209P (a) and gram-negative bacteria *Escherichia coli* ATCC 25922 (b) and powder samples ZnMgCu (samples 1) and ZnMgMn (samples 2). Bacteria-free zones around all powder samples are observed in these photos. The data of the average thicknesses of observed zones free from bacteria are given in Table 7.

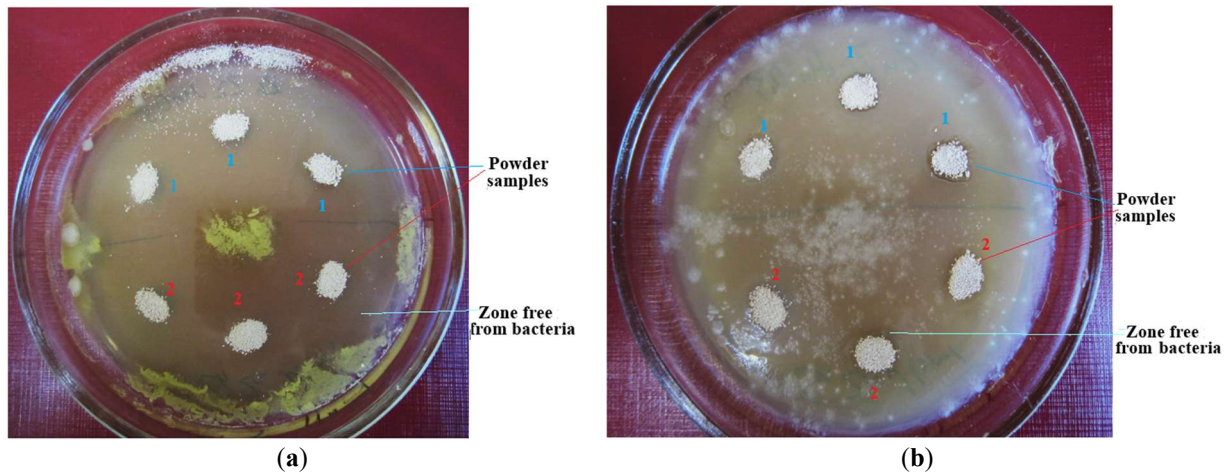


Figure 8. (a) Photo of Petri dish with agar containing gram-positive bacteria *Staphylococcus aureus* ATCC 209P and powder samples ZnMgCu (samples 1) and ZnMgMn (samples 2). (b) Photo of Petri dish with agar containing gram-negative bacteria *Escherichia coli* ATCC 25922 and powder samples ZnMgCu (samples 1) and ZnMgMn (samples 2).

Table 7. The average thicknesses of observed zones free from bacteria.

| Sample | Average Thickness of Zones Free from Bacteria, mm | |
|--------|---|------------------------------------|
| | <i>Staphylococcus aureus</i> ATCC 209P | <i>Escherichia coli</i> ATCC 25922 |
| ZnMgCu | 14.0 | 1.0 |
| ZnMgMn | 13.7 | 1.0 |

The thicknesses of the zones free from the bacteria *Staphylococcus aureus* ATCC 209P (Figure 7a) are significantly bigger than that observed for the bacteria *Escherichia coli* ATCC 25922 (Figure 7b). This fact can be related to the difference in the structure of these bacteria.

The obtained data show that prepared composites demonstrate high antibacterial activity against gram-positive bacteria *Staphylococcus aureus* ATCC 209P. However, their activity against gram-negative bacteria *Escherichia coli* ATCC 25922 is relatively weak.

4. Conclusions

Photocatalytic and bactericidal ZnO-MgO nanocomposites doped with Cu and Mn were synthesized by the simple polymeric sol-gel method. The crystal structures, morphologies, spectral and luminescence properties of prepared materials were studied. Obtained nanocomposites consist of small ZnO and MgO nanocrystals (sizes of ZnO crystals in both composites 18 nm) and have porous structure.

The analysis of diffuse reflection spectra showed that the band gap values of nanocomposites are higher than the band gap value of pure ZnO (3.42 and 3.41 eV for ZnO-MgO composites doped with Cu and Mn, correspondingly).

Both composites demonstrate the high ability of the photogeneration of chemically active singlet oxygen under blue light ($\lambda = 405$ nm) irradiation. The dependencies of the intensity of singlet oxygen photogeneration by composites from the power density of excited light are close to linear.

Photocatalytic decomposition of the Chicago Sky Blue diazo dye in solutions occurs fast in the presence of the prepared composites and at approximately the same rate (constants rate of photocatalytic dye decomposition are 0.024 min^{-1} and 0.025 min^{-1} for ZnO-MgO composites doped with Cu and Mn, correspondingly).

Prepared composites demonstrate high antibacterial activity against gram-positive bacteria *Staphylococcus aureus* ATCC 209P. However, their activity against gram-negative bacteria *Escherichia coli* ATCC 25922 is relatively weak.

Synthesized nanocomposites have similar characteristics and can be further used to clean the environment from organic pollutants.

Author Contributions

All authors contributed to the study conception and design. Material preparation, data collection and analysis were performed by A.S., A.K. and M.G. The first draft of the manuscript was written by S.E. and all authors commented on previous versions of the manuscript. The analysis and calculation of the specific surface area using the BET method were carried out by V.S. All authors read and approved the final manuscript.

Ethics Statement

Not applicable.

Informed Consent Statement

Not applicable.

Data Availability Statement

All data generated or analysed during this study are included in this published article.

Funding

The study was partly supported by Russian Science Foundation (project No. 20-19-00559).

Declaration of Competing Interest

The authors have no relevant financial or non-financial interests to disclose.

References

1. Turchi CS, Ollis DF. Photocatalytic Degradation of Organic Water Contaminants: Mechanisms Involving Hydroxyl Radical Attack. *J. Catal.* **1990**, *122*, 178–192.
2. Bell S, Will G, Bell J. Light intensity effects on photocatalytic water splitting with a titania catalyst. *Int. J. Hydrogen Energy* **2013**, *38*, 6938–6947.
3. Toshiro D, Yoshio N. Formation and behavior of singlet molecular oxygen in TiO₂ photocatalysis studied by detection of near-infrared phosphorescence. *J. Phys. Chem. C* **2007**, *111*, 4420–4424.
4. Zhang X, Qin J, Xue Y, Yu P, Zhang B, Wang L, et al. Effect of aspect ratio and surface defects on the photocatalytic activity of ZnO nanorods. *Sci. Rep.* **2014**, *4*, 4596.
5. Li Y, Zhang W, Niu J, Chen Y. Mechanism of Photogenerated Reactive Oxygen Species and Correlation with the Antibacterial Properties of Engineered Metal-Oxide Nanoparticles. *ACS Nano* **2012**, *6*, 5164–5173.
6. Wang D, Zhao L, Ma H, Zhang H, Guo L-H. Quantitative analysis of reactive oxygen species photogenerated on metal oxide nanoparticles and their bacteria toxicity: the role of superoxide radicals. *ACS Nano* **2017**, *51*, 10137–10145.
7. Liu D, Lv Y, Zhang M, Liu Y, Zhu Y, Zong P, et al. Defect-related photoluminescence and photocatalytic properties of porous ZnO nanosheets. *J. Mater. Chem. A* **2014**, *2*, 15377–15388.
8. Gavrilova MA, Gavrilova DA, Evstropiev SK, Shelemanov AA, Bagrov IV. Porous Ceramic ZnO Nanopowders: Features of Photoluminescence, Adsorption and Photocatalytic Properties. *Ceramics* **2023**, *6*, 1667–1681.
9. Wang T, Tian B, Han B, Ma D, Sun M, Hanif A, et al. Recent advances on porous materials for synergetic adsorption and photocatalysis. *Energy Environ. Mater.* **2022**, *5*, 711–730.
10. Shelemanov AA, Evstropiev SK, Karavaeva AV, Nikonorov NV, Vasilyev VN, Podruhin YF, et al. Enhanced singlet oxygen photogeneration by bactericidal ZnO–MgO–Ag nanocomposites. *Mater. Chem. Phys.* **2022**, *276*, 125204.
11. Deng Y. Developing a Langmuir-type excitation equilibrium equation to describe the effect of light intensity on the kinetics of the photocatalytic oxidation. *Chem. Eng. J.* **2018**, *337*, 220–227.

12. Puma GL, Salvadó-Estivill I, Obee TN, Hay SO. Kinetics rate model of the photocatalytic oxidation of trichloroethylene in air over TiO₂ thin films. *Sep. Purif. Technol.* **2009**, *67*, 226–232.
13. Ranjbari A, Demeestere K, Verpoort F, Kim K-H, Heynderick PM. Novel kinetic modeling of thiabendazole removal by adsorption and photocatalysis on porous organic polymers: Effect of pH and visible light intensity. *Chem. Eng. J.* **2022**, *431*, 133349.
14. Chi W, Yu F, Dong G, Zhang W, Chai D-F, Han P, et al. A novel peony-shaped ZnO/biochar nanocomposites with dominant {100} facets for efficient adsorption and photocatalytic removal of refractory contaminants. *Colloids Surf. A Physicochem. Eng. Asp.* **2024**, *695*, 134291.
15. Yang J, Wang L, Yang J, Li C, Zhong S. Magnetic biochar coupled with bismuth tungstate for multiple antibiotic removal from contaminated water: characteristics, performance, and competitive adsorption synergistic photocatalysis mechanism. *J. Environ. Chem. Eng.* **2024**, *12*, 111768.
16. Gavrilova M, Gavrilova D, Kondrashkova I, Evstropiev S. Structural engineering of nanocrystalline Zn_{0.5}Ni_{0.5}Fe₂O₄ synthesized by auto combustion method through the use of different organic reducing compounds and its effect on magnetic and photocatalytic properties. *J. Mater. Sci. Mater. Electron.* **2023**, *34*, 1644.
17. Choo-pun S, Vispute RD, Yang W, Sharma RP, Venkatesan T. Realization of band gap above 5.0 eV in metastable cubic-phase Mg_xZn_{1-x}O alloy films. *Appl. Phys. Lett.* **2002**, *80*, 1529–1531.
18. Shelemanov A, Tincu A, Evstropiev SK, Nikonorov N, Vasilyev V. Cu-doped porous ZnO-ZnAl₂O₄ nanocomposites synthesized by polymer-salt method for photocatalytic water purification. *J. Compos. Sci.* **2023**, *7*, 263.
19. Huang Z, Zheng X, Yan D, Yin G, Liao X, Kang Y, et al. Toxicological effect of ZnO nanoparticles based on bacteria. *Langmuir* **2008**, *24*, 4140–4144.
20. Chabri S, Dhara A, Show B, Adak D, Sinha A, Mukherjee N. Mesoporous CuO-ZnO p-n heterojunction based nanocomposites with high specific surface area for enhanced photocatalysis and electrochemical sensing. *Catal. Sci. Technol.* **2016**, *6*, 3238–3252.
21. Kargar A, Jing Y, Kim SJ, Riley CT, Pan X, Wang D. ZnO/CuO heterojunction branched nanowires for photoelectrochemical hydrogen generation. *ACS Nano* **2013**, *7*, 11112–11120.
22. Panchal P, Sharma R, Reddy AS, Nehra K, Sharma A, Nehra SP. Eco-friendly synthesis of Ag-doped ZnO/MgO as a potential photocatalyst for antimicrobial and dye degradation applications. *Coord. Chem. Rev.* **2023**, *493*, 215283.
23. Li J, Nie X, Meng L, Zhang X, Bai L, Chai D-F, et al. Microwave-assisted hydrothermal synthesis of Ag/Bi₂MoO₆/ZnO heterojunction with nano Ag as electronic accelerator pump for high-efficiency photocatalytic degradation of levofloxacin. *Appl. Surf. Sci.* **2024**, *678*, 161143.
24. Hamrouni A, Moussa N, Parrino F, Di Paola A, Houas A, Palmisano L. Sol-gel synthesis and photocatalytic activity of ZnO-SnO₂ nanocomposites. *J. Mol. Catal. A Chem.* **2014**, *390*, 133–141.
25. Zhu L, Hong M, Ho GW. Hierarchical assembly of SnO₂/ZnO nanostructures for enhanced photocatalytic performance. *Sci. Rep.* **2015**, *5*, 11609.
26. Etacheri V, Roshan R, Kumar V. Mg-doped ZnO nanoparticles for efficient sunlight-driven photocatalysis. *ACS Appl. Mater. Interfaces* **2012**, *4*, 2717–2725.
27. Vijayalakshmi K, Karthick K. Growth of highly c-axis oriented Mg: ZnO nanorods on Al₂O₃ substrate towards high-performance H₂ sensing. *Int. J. Hydrogen Energy* **2014**, *39*, 7165–7172.
28. Nishimoto N, Yoshino K, Fujihara J, Kitahara K. Evaluation of ZnO-MgO mixed thin films grown by metal-organic decomposition. *e-J. Surf. Sci. Nanotechnol.* **2015**, *13*, 185–189.
29. Balta AK, Ertek Ö, Eker N, Okur I. MgO and ZnO composite thin films using the spin coating method on microscope glasses. *Mater. Sci. Appl.* **2015**, *6*, 40–47.
30. Caglar M, Wu J, Li K, Caglar Y, Ilican S, Xue D. Mg_xZn_{1-x}O (x= 0–1) films fabricated by sol-gel spin coating. *Mater. Res. Bull.* **2010**, *45*, 284–287.
31. Panchal P, Paul DR, Sharma A, Hooda D, Yadav R, Meena P, et al. Phytoextract mediated ZnO/MgO nanocomposites for photocatalytic and antibacterial activities. *J. Photochem. Photobiol. A Chem.* **2019**, *385*, 112049.
32. Deng H, Fei X, Yang Y, Fan J, Yu J, Cheng B, et al. S-scheme heterojunction based on p-type ZnMn₂O₄ and n-type ZnO with improved photocatalytic CO₂ reduction activity. *Chem. Eng. J.* **2021**, *409*, 127377.
33. Senol SD, Boyraz C, Ozugurlu E, Gungor A, Arda L. Band Gap Engineering of Mg Doped ZnO Nanorods Prepared by a Hydrothermal Method. *Cryst. Res. Technol.* **2019**, *54*, 1800233.
34. Bulyga DV, Evstropiev SK. Kinetics of adsorption and photocatalytic decomposition of a diazo dye by nanocomposite ZnO-MgO. *Opt. Spectrosc.* **2022**, *130*, 1176–1184.
35. Bulyga DV, Evstropiev SK, Nashchekin AV. Structural engineering of ZnO-MgO intermediates for functional ceramics. *Res. Chem. Intermed.* **2022**, *48*, 4785–4796.
36. Tsay C-Y, Wang M-C, Chiang S-C. Effects of Mg additions on microstructure and optical properties of sol-gel derived ZnO thin films. *Mater. Trans.* **2008**, *49*, 1186–1191.

37. Bhattacharya P, Das RR, Katiyar RS. Comparative study of Mg doped ZnO and multilayer ZnO/MgO thin films. *Thin Solid Films* **2004**, 447–448, 564–567.
38. Gupta KK, Tan C-P, Hsu C-M, Lin B-C, Lu C-H. Bio-polymer agar-assisted sol-gel synthesis and electrochemical characterization of bi-pyramidal $\text{LiNi}_{0.8}\text{Co}_{0.1}\text{Mn}_{0.1}\text{O}_2$ cathode materials for lithium-ion batteries. *J. Sol-Gel Sci. Technol.* **2023**, 108, 685–694.
39. Sangeeta M, Karthik KV, Ravishankar R, Anantharaju KS, Nagabhushana H, Jeetendra K, et al. Synthesis of ZnO, MgO and ZnO/MgO by Solution Combustion Method: Characterization and Photocatalytic Studies. *Mater. Today Proc.* **2017**, 4, 11791–11798.
40. Davis K, Yarbrough R, Froeschle M, White J, Rathnayake H. Band gap engineered zinc oxide nanostructures via a sol-gel synthesis of solvent driven shape-controlled crystal growth. *RSC Adv.* **2019**, 9, 14638–14648.
41. Kumar P, Khatri T, Bawa H, Kaur J. ZnO-Fe₂O₃ heterojunction for photocatalytic degradation of victoria blue dye. *AIP Conf. Proc.* **2017**, 1860, 020065.
42. Cheng L, Liu L, Li R, Zhang J. Liquid phase deposition of $\alpha\text{-Fe}_2\text{O}_3/\text{ZnO}$ heterojunction film with enhanced visible-light photoelectrocatalytic activity for pollutant removal. *J. Electrochem. Soc.* **2017**, 164, H726.
43. Tanaka K, Padermpole K, Hisanaga T. Photocatalytic degradation of commercial azo dyes. *Water Res.* **2000**, 34, 327–333.
44. Riaz N, Hassan M, Siddique M, Mahmood Q, Farooq U, Sarwar R, et al. Photocatalytic degradation and kinetic modeling of azo dye using bimetallic photocatalysts: effect of synthesis and operational parameters. *Environ. Sci. Pollut. Res.* **2020**, 27, 2992–3006.
45. Klein J, Kampermann L, Mockenhaupt B, Behrens M, Strunk J, Bacher G. Limitations of the Tauc plot method. *Adv. Funct. Mater.* **2023**, 33, 2304523.
46. Evstropiev SK, Vasilyev VN, Nikonorov NV, Kolobkova EV, Volkova NA, Boltenev IA. Photoactive ZnO nanosuspension for intensification of organics contaminations decomposition. *Chem. Eng. Process. Process Intensif.* **2018**, 134, 45–50.
47. Shannon RD. Revised effective ionic radii and systematic studies of interatomic distances in halides and chalcogenides. *Acta Crystallogr. A* **1976**, 32, 751–767.
48. Mohammad A, Kapoor K, Mobin SM. Improved photocatalytic degradation of organic dyes by ZnO-nanoflowers. *ChemSelect* **2016**, 1, 3483–3490.
49. Chitradevi T, Jestin Lenus A, Victor Jaya N. Structure, morphology and luminescence properties of sol-gel method synthesized pure and Ag-doped ZnO nanoparticles. *Mater. Res. Express* **2020**, 7, 015011.
50. Ma Z, Ren F, Ming X, Long Y, Volinsky AA. Cu-doped ZnO electronic structure and optical properties studied by first-principles calculations and experiments. *Materials* **2019**, 12, 196.
51. Bilgili O. The Effects of Mn Doping on the Structural and Optical Properties of ZnO. *Acta Phys. Pol. A* **2019**, 136, 460–466.
52. Mediouni N, Guillard C, Dappozze F, Khrous L, Parola S, Colbeau-Juatin C, et al. Impact of structural defects on the photocatalytic properties of ZnO. *J. Hazard. Mater. Adv.* **2022**, 6, 100081.